ARTICLE

Effect of thermal cycles on the laser beam welded joint of AA2060 alloys

Ling Mao
School of Materials Science and Engineering, Beihang University (BUAA), Beijing 100191, People's Republic of China

Huijin Jin
State Key Laboratory of Nonlinear Mechanics, Institute of Mechanics, Chinese Academy of Sciences, Beijing 100191, People's Republic of China

Fan Ye and Feifei Wang
School of Materials Science and Engineering, Beihang University (BUAA), Beijing 100191, People's Republic of China

Gang Zheng
Central Research Institute, Principle Engineer State Nuclear Power Technology Co. Ltd., Beijing 102209, People's Republic of China

Sujun Wu[a)]
School of Materials Science and Engineering, Beihang University (BUAA), Beijing 100191, People's Republic of China

(Received 10 March 2018; accepted 22 June 2018)

The effects of the thermal cyclic aging treatment on the microstructure and mechanical properties of 2060 Al–Li alloy laser beam welded joints were investigated. Aging treatments were conducted at different temperatures and for different cycles. Test results showed that the tensile strength of the weld joints increased and the elongation slightly decreased after the thermal cycling treatment. It was also found that the heat affected zone (HAZ) of the welds exhibited a significant increase in microhardness, whilst the microhardness variation of the nondendrite equiaxed zone (EQZ) can be neglected. The strengthening effect of the thermal cycling became more obvious as the temperature and cycles increased. The highest strength of around 513 MPa (96% of the base metal) was obtained at the temperature of 180 °C. Reprecipitation of strengthening phases such as T1 in the HAZ at 180 °C was observed by TEM, which can be considered as the main reason for the strengthening effect of the aging treatment.

I. INTRODUCTION

High-performance light alloys have been widely used in industry due to their lightweight and remarkable specific properties.[1–4] Adding lithium to aluminum alloys is a common way to reduce alloy density and increase its specific modulus. The newly developed 2060 Al–Li alloy possesses good ductility and excellent resistance to fatigue and corrosion.[5] This type of new generation Al–Li alloy can be applied to the aerospace industry to replace the traditional Al alloy 2XXX and 7XXX series.[3,4,6] Another important factor for the novel alloy practical use is the joining technique. Riveting is the most widely used technique for aircraft parts joining nowadays. However, the application of laser beam welding (LBW) is gradually replacing the traditional riveting method, which becomes one of the most important techniques for Al–Li alloy joining. A narrow heat affected zone (HAZ) with lower distortion can be achieved by LBW, thanks to the tight focus ability and high power density of laser beam.[7] Compared with riveting and arc welding, the structural integrity and mechanical properties of the LBW joints are highly improved. The excellent flexibility and accessibility of LBW with no vacuum requirement has broadened its application range. It has already been used for welding of various alloys such as 5A09, 8090, 1420, 2A97, and 2090.[8–12]

The effects of LBW on the microstructure and mechanical properties of the 2060 alloy have been widely studied in the past decade.[13,14] The welding porosity, hot cracking, and weld softening are the main problems during welding.[7,9,15,16] Many researchers who focus on the optimization of welding parameters and prewelding treatment have found methods to improve the material performance, such as removing oxide film, adjusting the welding speed, adding the filler wire, and inventing double-sided LBW.[17–20] As shown in previous research

[a)]Address all correspondence to this author.
e-mail: wusj@buaa.edu.cn
DOI: 10.1557/jmr.2018.229

studies, the post-weld heat treatment (PWHT) can be applied on the joints welded by tungsten-inert-gas,[21–23] electron-beam-welding,[24,25] or friction-stir-welding[26] to improve the mechanical properties of weld joints and meet the practical requirements. However, there are few reports about the application of PWHT on the LBW Al–Li alloy, not to mention the thermal cycling treatment.[27,28] Cui et al.[27] developed the solution-aging treatment on 5A09 alloys after LBW. It was demonstrated that the PWHT improved the microstructure uniformity and enhanced the hardness of weld but reduced the microhardness of base metal. The process of thermal cyclic aging is to conduct artificial aging for several cycles after welding. The absence of solution heat treatment could reduce the effects of PWHT on base metal. Xu et al.[28] stated that the strength of the welds can increase after single artificial aging, although the effect was less than the effect of solution-aging treatment. The slow heating and cooling processes during artificial aging were found to influence the precipitation of the second phase particles,[29] which can be considered as the non-isothermal aging effect. Li et al.[30] proved that non-isothermal aging could slow the aging kinetics to enhance the strengthening effect. The results showed that comparing to isothermal aging, nonisothermal aging improved the tensile strength without decreasing the elongation.[29] Thus, it could be beneficial to apply the thermal cyclic aging treatment to the Al–Li alloy welded by laser beam, aiming to obtain the sound joints.

The aim of this investigation is to study the influences of thermal cyclic aging treatment on the precipitates and mechanical properties for laser-welded 2060 joints. Different aging temperatures and cycles were applied and the corresponding microstructure, microhardness, and tensile strength of weld joints were investigated.

II. EXPERIMENTAL SECTION

AA2060 alloy sheets with a thickness of 2.0 mm were received in the T8 state, i.e., artificially aged after solution heat-treatment and cold deformation. The base metal was welded by LBW to obtain T-lap joint, with the 2196 alloy serving as ribbed slab. The welding direction was parallel to the rolling direction of the AA2060 alloy. The chemical composition of the alloys is given in Table I.

The thermal-cycling aging was conducted in the blast air oven (DHG-9245AD, LABFREEZ, Beijing, China). Different aging temperatures 110 °C, 130 °C, 150 °C, and 180 °C, with 3 and 5 aging cycles, respectively, were applied for comparison. The heating/cooling rate was controlled at 20 °C/h and the aging time was kept for 4 h (Fig. 1).

The grain morphology and precipitates of the 2060-T8 alloy and weld joints were observed by using OM (Leica DM4000M, Leica, Solms, Germany) and TEM (JOEL JEM-2010F, JEOL, Tokyo, Japan), respectively. OM specimens were cut vertical to the weld and etched by using the Keller's reagent for 10 s. The cross-sectional welds were sliced to the desired thickness of 0.4 mm and then ground to 30 μm thick. Thinned areas for TEM observation were produced by ion milling with chemical solution of 25 vol% nitric acid in methanol (75 vol%) at 248 K. Vickers microhardness tests were carried out to measure the hardness of distinct zones across the weld joints with a load of 10 g and a dwell time of 15 s. Subsize samples for transverse tensile testing were cut by wire-cut electrodischarged machining. The dimensions and gauge length were determined as shown in Fig. 2. Five specimens in each condition were tested with the strain rate of 0.04 mm/mm/min at ambient temperature to evaluate the mechanical properties.

III. RESULTS AND DISCUSSION

A. Grain morphology

Figure 3 presents the optical micrograph of the weld joints near the fusion boundary under different heat treatment conditions. The laser welding joint consists of three parts: HAZ, EQZ, and NZ. As the grain morphology showed [Fig. 3(a)], the NZ was divided into column dendrite zone and equiaxed dendrite zone. Occasionally, the nondendrite grain band was observed in the NZ. The difference in grains is due to the competition between the super cooling degree and atomic diffusion speed in distinct zones.

The EQZ, a feature distinguished from other traditional aluminum alloys, is a hot issue in fusion weld of the Al–Li alloy. The EQZ was located around the fusion boundary and occasionally found in the NZ. As Gutierrez et al.[31] stated, the mechanism of fine equiaxed grains is nucleation-growth hypothesis. The heterogeneous nuclei were identified as Al_3Zr and $Al_3(Li_x, Zr_{1-x})$, which were still retained after the heating process of welding. The

TABLE I. Chemical composition of AA2060 and 2196 alloys.

	Element (wt%)							
Alloy	Li	Cu	Mg	Zr	Mn	Zn	Ag	Others
2060	0.7	3.7	0.7	0.11	0.3	0.4	0.3	...
2196	1.4–2.1	2.5–3.3	0.25–0.8	0.04–0.18	<0.35	<0.35	0.25–0.6	Ti < 0.01

precipitation distribution of EQZ is displayed in Fig. 3(b). There were a few spherical/cubic precipitates and dense dislocations observed inside the grains. The precipitates were considered as Al_3Zr by the analysis of an energy dispersive spectrometer, which was supported by the nucleation-growth mechanism. Some impurity phases containing Al, Cu, Fe, and Mn were aligned along the grain boundary, due to the solute segregation.[12] Note that the coarsening of the grain morphology was not obvious in the HAZ, which was due to the low heat input in LBW. In terms of the grain morphology, little difference was found in the weld after thermal cyclic aging. The diffusion of Al atoms was limited at the aging treatment temperatures which are not high enough to cause grain growth.

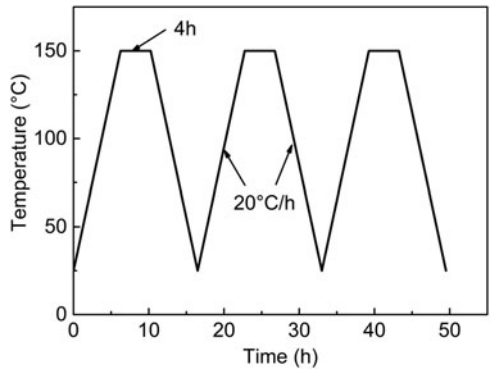

FIG. 1. Schematic diagram of thermal-cycling aging.

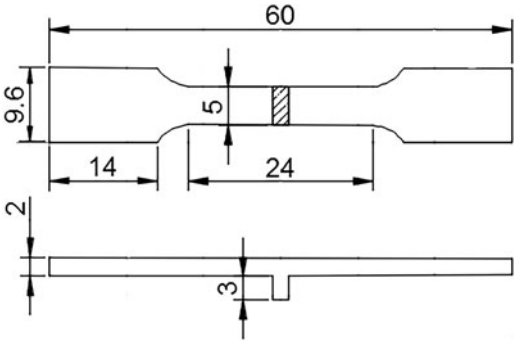

FIG. 2. Dimensions of tensile testing specimens, mm.

B. Microhardness

The microhardness distribution of as-received weld joints was represented by the "U"-shaped profile in Fig. 4, which was similar to the results obtained by Tao et al.[13,14] The HAZ-1 and HAZ-2 represent the HAZ near the base metal of 2060 and 2196 alloys, respectively. The average microhardness values of the 2060 and 2196 BMs were ~168 and ~165 HV, while that of the NZ was approximately 110 HV, much lower than that of the base metal. The low NZ hardness value may result from the loss of alloy elements in the weld pool and the impediment to precipitation of the strengthening precipitates due to fast solidification. Since the original precipitates would dissolve under the influence of the heat input during welding, the microhardness of HAZs was also lower than that of the BM. Due to the microstructure difference between 2060 and 2196 alloys, the HAZ-1 (~130 HV) showed higher microhardness than HAZ-2 (~111 HV) close to the fusion line. The microhardness value of the EQZ was lowest, about 103 HV, although the grain of the EQZ was less than 10 μm [Fig. 3(a)]. It was due to the lack of a large number of precipitates in the EQZ as shown in Fig. 3(b).

The microhardness of the T-shaped joints subjected to different thermal cycling treatments is shown in Fig. 4. Figures 4(a) and 4(b) represent the effect of 3 and 5 aging cycles, respectively. The variation trend of the hardness with the aging temperature for 3 cycles was similar to 5 cycles, roughly. It can be seen that the microhardness in the HAZs increased with the increase of aging temperature while the variation in the NZ was insignificant. The microhardness increment of the HAZ after thermal cycling aging at 110 and 130 °C remained same for both 3 cycles and 5 cycles, indicating that the strengthening effect was saturated after 3 aging cycles at these two relatively lower temperatures. When aging at 150 °C, the

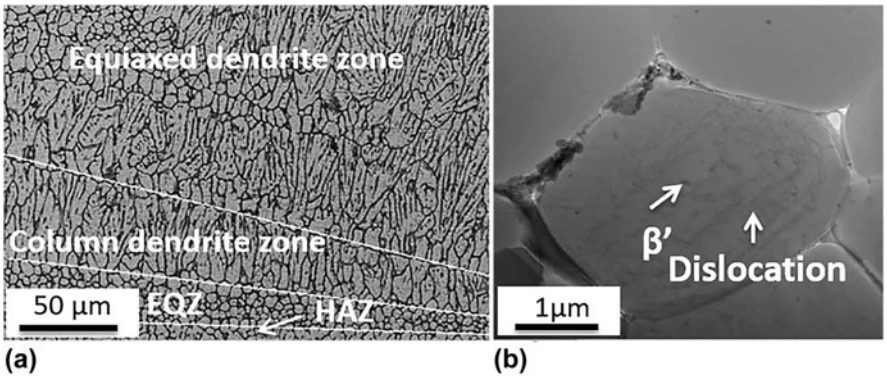

FIG. 3. (a) Optical image of the whole weld joint. (b) STEM image of the EQZ showing existence of dense dislocation and a few precipitates.

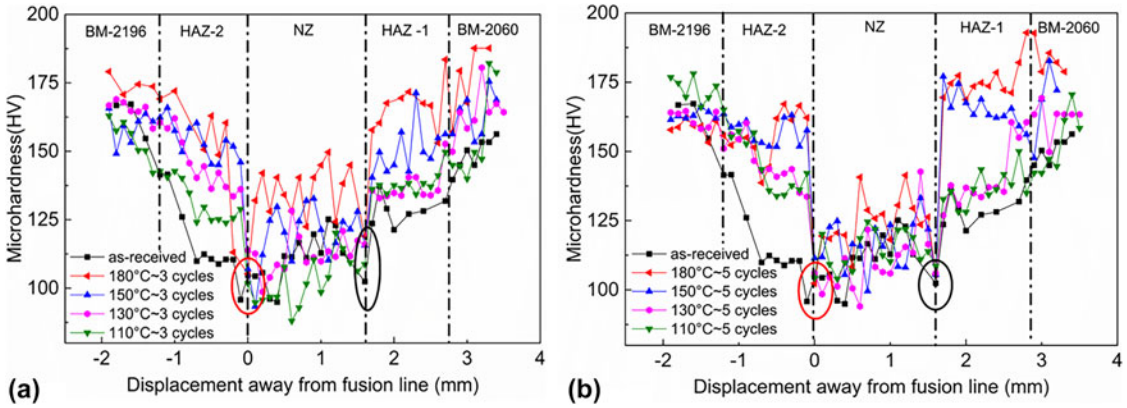

FIG. 4. Microhardness distribution profile of the weld joint. (a) 3 cycles and (b) 5 cycles, respectively, at different elevated temperatures.

microhardness of the HAZ for 5 cycles was significantly higher and closer to the value aged at 180 °C, as compared to 3 cycles. It implies that at 150 °C, the strengthening effect of thermal cyclic aging did not reach saturation after 3 cycles but close to saturation after 5 cycles. The variation at 180 °C of microhardness for different cycles was less significant compared with the effect at 150 °C, meaning that the strengthening effect was close to saturation after 3 cycles at 180 °C. The different aging effect on microhardness of the HAZs between the relatively higher temperature (150 and 180 °C) and the relatively lower temperature (130 and 110 °C) demonstrates that different strengthening mechanisms were in action during the aging treatment. The most significant effect of thermal cyclic aging on the weld joints was found at aging temperature of 180 °C.

For natural aging and the early stage of artificial aging, the main precipitates of the Al–Li alloy are G.P. zone, θ′(Al_2Cu), and δ′(Al_3Li) phase. The precipitation temperature of these phases ranges from 60 to 110 °C.[32] In our study, the aging temperature of 110 and 130 °C was high enough for the quick formation of θ′ and δ′ phases. It seems that the precipitation process was completed within 3 aging cycles, and further extension of aging time to 5 cycles did not make great difference to the precipitates; therefore, the hardness did not have obvious change in the HAZ below 130 °C. When the aging temperature is between 135 and 260 °C, the predominant strengthening phase of the Al–Li alloy is the T1 (Al_2CuLi) phase with a small amount of the σ phase.[33] As mentioned above, the effect of the aging cycles was more obvious in the HAZ when the aging temperature was higher (above 150 °C), indicating different strengthening mechanisms. It could be attributed to the formation of the strengthening phase, the T1 phase, which can only form at relatively higher aging temperature. Adrell et al.[34] reported that the precipitation and growth of the T1 phase was at the expense of the δ′ phase at the early aging stage, while both θ′ and δ′ phases were consumed at the peak aging stage. The core of the competition was Li and Cu atoms. Different precipitates generate strengthening effects with different mechanisms. The δ′ phase possesses a L12 structure coherent with the matrix, which could be easily cut through by the dislocations during deformation.[35] The T1 phase is semicoherent with the matrix, which has the high distortion energy. The interaction between the dislocations and T1 phase is the mixture of cutting and bypassing mechanism,[36] leading to the more obvious strengthening effect at higher aging temperature. After the aging treatment of 3 cycles at 150 °C, the precipitation did not reach saturation. The increase of the aging cycles promotes more precipitation and then improved the microhardness in the HAZ further. Once the aging temperature increased to 180 °C, the precipitation was close to saturation after 3 cycles. Thus, the less improvement of microhardness was found at the temperature of 180 °C with the increase of the aging to 5 cycles.

As shown in Fig. 4, the EQZ had the lowest microhardness value which remained unchanged with the aging treatment. According to Fu et al.,[12] the alloying elements, such as Cu, segregated onto the grain boundaries in the EQZ, which weakened the precipitation ability of the strengthening phases during the aging treatment. As a result, the strengthening effect of the thermal aging heat-treatment on the hardness of the EQZ can be neglected. According to Sidhar et al.,[37] the low dislocation density of the NZ retards the precipitation of T1 phases. Thus, the microhardness of the NZ exhibited insignificant change after thermal cyclic aging. In addition, when the aging temperature was relatively low (110 and 130 °C), the aging treatment had more significant influence on the microhardness of the HAZ-2 than that of the HAZ-1. The difference of sharp jump in the two HAZs could be explained by the effect of chemical composition differences on the precipitation of the strengthening phases. As can be seen from Table I, the main difference in chemical elements of the two alloys

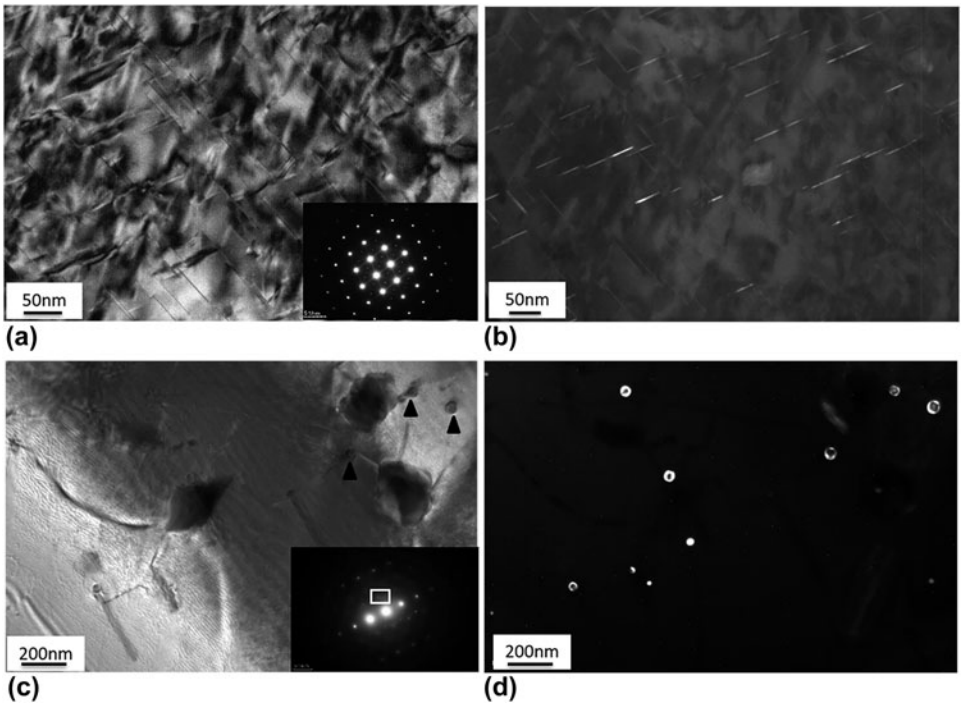

FIG. 5. TEM micrographs of the base metal (a and b) and HAZ of the as-received weld (c and d). (a) Bright field image of the base metal and the inset is the SAD pattern with the [110] matrix zone. (b) DF image of the T1 phase. (c) Bright field image of the HAZ near fusion line and the inset is the SAD pattern near the [311] matrix zone. (d) DF image of weak spots marked in (c).

lies in the Cu/Li ratio. The high Cu/Li ratio could suppress the formation of the δ′ phase.[38] Due to the low content Li and high Cu/Li ratio in the 2060 alloy, it was more difficult for the precipitation of the δ′ phase in the HAZ-1 near the 2060 alloy during thermal cyclic aging. When the aging temperature was relatively low, the δ′ and θ′ phases were the main strengthening phases. As a result, the increment of the microhardness in the HAZ-1 was smaller than that of the HAZ-2 after the aging treatment at 110 and 130 °C.

C. Precipitates

The TEM micrographs of 2060 base metal are presented in Fig. 5. It was observed that needle-shaped phases were uniformly distributed in the base metal [Fig. 5(a)]. The spots from $1/3\langle 220\rangle_{Al}$ and streaks forming the sides of the rhombus revealed the presence of the T1 phase. Combined with the dark field (DF) image of the spots [Fig. 5(b)], the needle phases can be confirmed as the T1 phase. As is shown in Fig. 5(b), two variants of T1 phases were uniformly distributed within interior grains rather than at subgrain boundaries. In addition, there were weak superlattice spots in the SAD pattern, implying the existence of a small amount of δ′ precipitates in the base metal [the inset of Fig. 5(a)].

The precipitation in the HAZ of the as-received weld was also obtained from TEM [Figs. 5(c) and 5(d)]. It was observed that some spherical nanometer phases were distributed disorderly in the HAZ. The corresponding SAD pattern is displayed in the inset of Fig. 5(c), which indicates that the spherical particles are the δ′ phase. It can be seen that some of the δ′ particles have a dark core which is believed to be the β′ particle, performing as the nuclei of the strengthening δ′ phases during aging treatment. There were no T1 phases found in the HAZ at the original weld state. The high cooling rate during the LBW welding process suppressed the precipitation of the T1 phases.[13,39] The T1 phase is the dominant strengthening phase in the Al–Cu–Li alloys.[39] The absence of T1 phase in the as-received weld explained the lower hardness of the HAZ than the 2060 base metal.

The HAZs of the weld joints after 5 cycles at 130 °C and 5 cycles at 180 °C were selected for TEM observation. The DF images in Figs. 6(a) and 6(b) demonstrated the precipitation of the strengthening phases after cycling aging treatment at 130 °C for 5 cycles. The relevant results of the SAD pattern with the $[211]_{Al}$ zone is shown in the inset of Fig. 6(a). Calculation and analysis of the SAD revealed that the particles in Fig. 6(a) are δ′ precipitates and the particles in Fig. 6(b) are θ′ precipitates. The TEM results of the HAZ after aging treatment at 180 °C for 5 cycles are displayed in Figs. 6(c) and 6(d), which contains large amount of needle phases and some spherical particles. The corresponding SAD pattern with the $[100]_{Al}$ zone [Fig. 6(c)] revealed the precipitation of

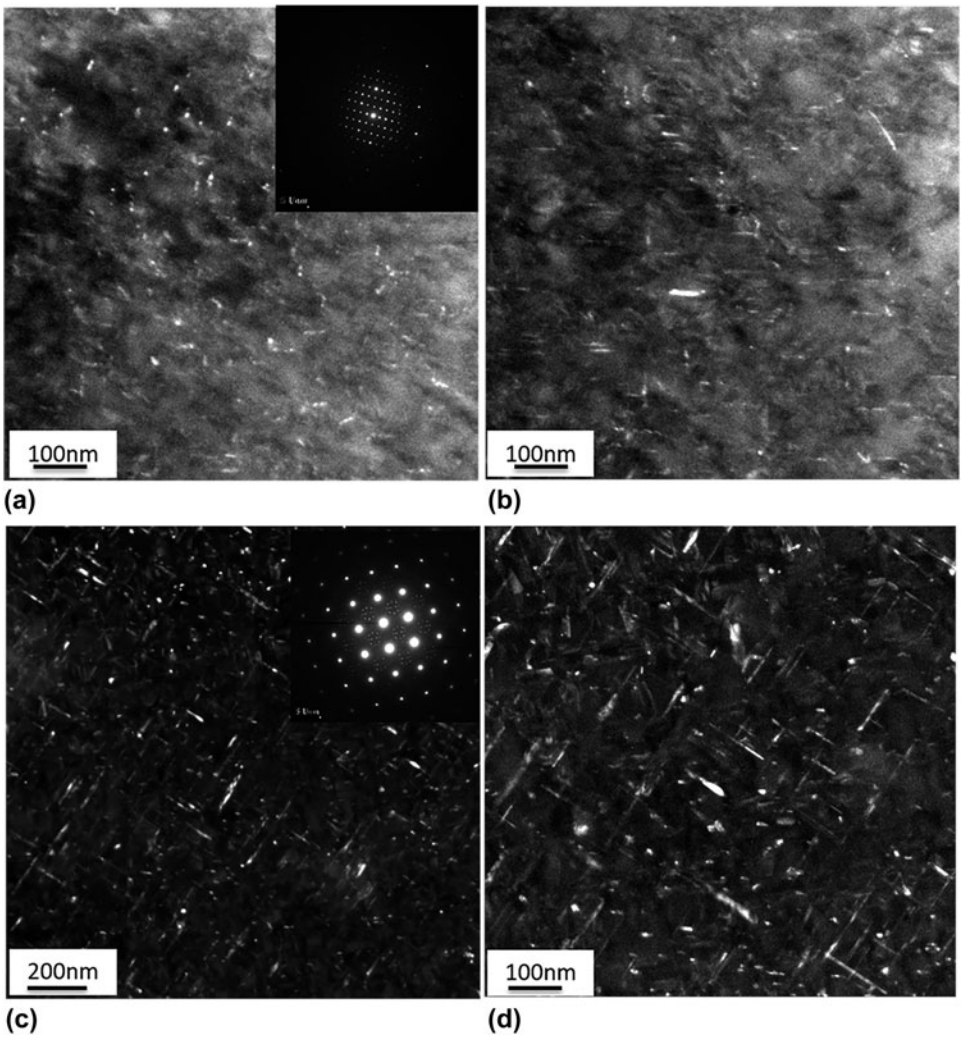

FIG. 6. TEM micrographs of HAZs after aging treatments. DF images of (a) δ′ phases and (b) θ′ phases for 5 cycles at 130 °C. The inset of (a) is the SAD pattern with the [211] matrix zone for 5 cycles at 130 °C. (c) DF images of T1 phases for 5 cycles at 180 °C. The inset is the SAD pattern with the [100] matrix. (d) The magnified image of T1 phases for 5 cycles at 180 °C.

needle-shaped T1 phases and the existence of δ′ particles after cycling aging at 180 °C. The four spots symmetrically distributed about intersection of the diagonals of a square related to the reflection of four variants of the T1 phase. In addition, the spots produced by the δ′ phase were weaker than that of the HAZ repeatedly aged at 130 °C [Fig. 6(b)]. The DF image in Fig. 6(d) represented the lenticular T1 phases. The precipitation of the strengthening phases was considered to improve the mechanical properties of the weld joints.

In contrast to the as-received weld HAZ, the thermal cyclic aging promoted the precipitation of strengthening phases such as θ′ phases, δ′ phases, and T1 phases. The main strengthening phases after thermal cyclic aging at lower temperature (110 and 130 °C) were θ′ and δ′ phases, which were responsible for the increment of microhardness in the HAZ after aging treatment. As the aging temperature increased up to 150 and 180 °C, the θ′ and δ′ precipitates transformed into the T1 phase. The formation of the new phases brought more obvious strengthening effect than the θ′ and δ′ precipitates. Thus, the microhardness in the HAZ after cycling aging at higher temperatures exhibited a dramatic increase, comparing to that after lower temperature aging treatment.

D. Tensile properties

The results of tensile strength and elongation are displayed in Figs. 7(a) and 7(b). The tensile strength of the as-received joint reached 406.86 MPa, about 76% of the 2060 base metal (~533 MPa). The result is analogous to the joint strength coefficient (the UTS ratio of the weld joint and base metal) reported for the 2A97 LBW joint.[12] The elongation of the as-received weld was about 2.1%, indicating a large reduction compared to the 16% of the 2060 BM. It can be seen from Fig. 7 that the tensile

strength of the weld joints increased with the aging temperature, while the elongation slightly decreased.

The weld joints subjected to thermal cyclic aging at 180 °C possessed the highest tensile strength, about 513 MPa (~96% of the 2060 BM strength). The strength values of the weld joints aged for both 3 cycles and 5 cycles at 180 °C were quite similar, probably due to the saturation of the strengthening effect of the T1 phase precipitation. When the aging temperature was relatively low (110 and 130 °C), the tensile strength of the weld joints exhibited slight improvement when the number of aging cycles extended to 5 cycles. As mentioned before, the strengthening phases at the relatively low temperature were θ′ and δ′ phases. The precipitation process could almost be completed within 3 cycles, implying that the strengthening effect was close to saturation. Thus, the effect of the extended cycling time on the strength of the weld joints could be ignored at 110 and 130 °C. As the aging temperature increased up to 150 °C, the difference of the tensile strengths between 3 cycles and 5 cycles was obvious. This means that the increase of the cycling numbers had significant influence on the tensile strength at 150 °C. As mentioned above, at 150 °C, the strengthening phases of θ′ and δ′ would be dissolved and a new strengthening phase of T1 would be formed. The transformation process, however, was not fast enough compared with that at 180 °C, and the precipitation of the T1 phase could not reach saturation after 3 cycles. When the cycles increased to 5 cycles, further precipitation of the strengthening phase enhanced the tensile strength remarkably. The variation of the tensile strengths after thermal cyclic aging was in good agreement with that of microhardness (see Fig. 4).

The fracture morphology of the 2060 BM was observed by SEM after tensile testing (Fig. 8). The obvious delamination was found on the fracture surface, as shown in Fig. 8(a). It is the characteristic of the Al–Li alloy fracture, implying the existence of the external reinforcement during tensile testing.[40] The external reinforcement could improve the ductility of the Al–Li alloy. In addition, it can be seen from Fig. 8(b) that there were many deep dimples on the fracture surface with some particles. On account of the delamination and dimples, the 2060 BM possessed good ductility and the 16% elongation was in line with it.

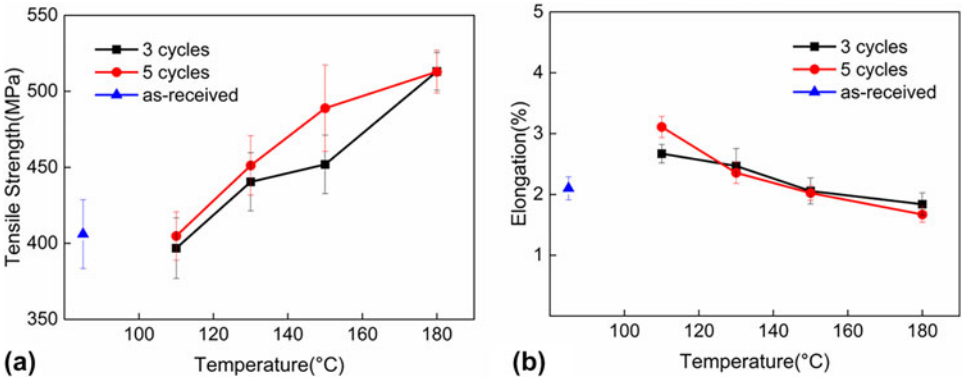

FIG. 7. Line chart representing the comparison of (a) tensile strength and (b) elongation in different conditions.

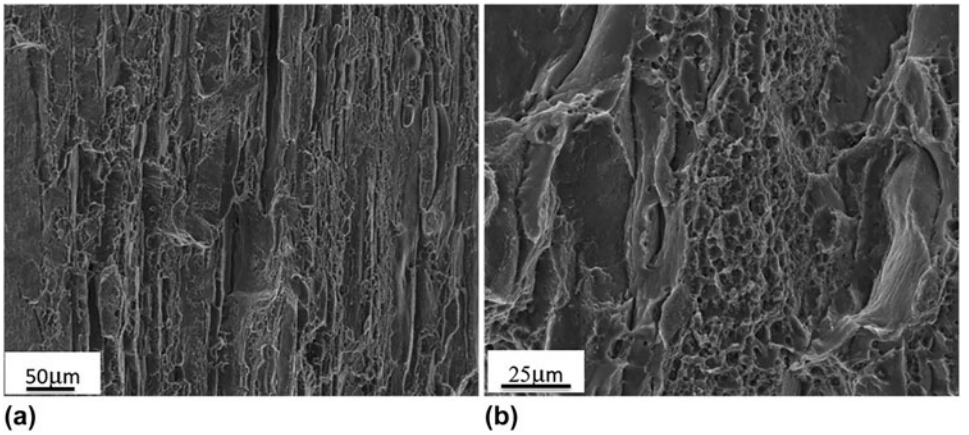

FIG. 8. SEM fracture images of the 2060 BM at the magnification of (a) 500× and (b) 1500×.

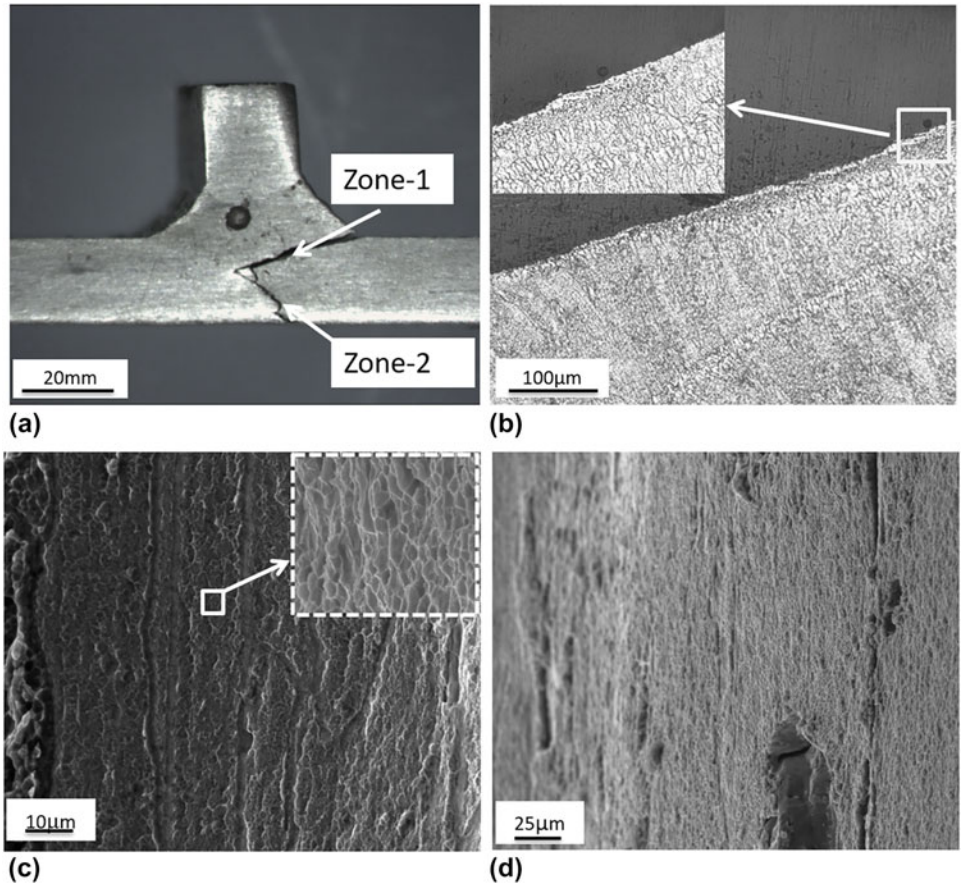

FIG. 9. (a) Stereo micrograph of the fracture weld joint. (b) OM images of the fracture surface. (c) SEM image of zone-1. The inset is the magnification of the dimples. (d) SEM image of the fracture showing weld defects.

The fracture observation results of the T-lap weld joints are displayed in Fig. 9. It can be concluded from Fig. 9(a) that the fracture of the weld consisted of two parts, zone-1 and zone-2. Zone-1 and zone-2 were the fracture surfaces near the weld metal and in the BM, respectively. The crack initiated in the weld toe on the skin panel, where the stress concentration was located. It was widely reported[12,41–43] that the EQZ was the weakest link for the Al alloy LBW joints and the grain boundaries of the EQZ were the easy path for the crack to grow. In the present work, however, it can be seen from Fig. 9(b) that the fracture path was mainly along the fusion line adjacent to the EQZ, but not within the EQZ, with some part in the HAZ. The SEM images of zone-1 are shown in Figs. 9(c) and 9(d). The inset of Fig. 9(c) exhibited the existence of the intensive dimples on the fracture surface of zone-1. At the same time, Fig. 9(d) reveals that there was a large amount of weld defects. The local dimples could not eliminate the negative effect of the defects on the weld ductility. Thus, the weld joints showed poor ductility during tensile testing. After reaching the point of the deepest penetration, the crack turned to the 2060 BM to continue propagation. The fracture mode of zone-2 was same with that of the 2060 BM. As the external force was applied to the remained BM, the weld joints fractured quickly.

IV. CONCLUSION

The thermal cyclic aging treatment at different temperatures and cycle numbers was conducted for the 2060 alloy T-shaped joint, which was welded by the LBW method. The joint strength coefficient of the as-received weld was 76%. The grain morphology, precipitation distributions, and mechanical properties were investigated to understand the effect of thermal cyclic aging. And the following conclusions can be drawn:

(1) The microhardness and tensile strength of the 2060 Al–Li alloy weld increased with the increase of the thermal cyclic aging temperature and cycles. The highest strength of around 513 MPa (96% of the base metal) was obtained at the temperature of 180 °C.

(2) The lower temperature aging promoted the formation and growth of δ' and θ' phases in the HAZ. As the aging temperature increased up to 150 and 180 °C, the T1

phase precipitated in the HAZ, resulting in higher microhardness and tensile strength.

(3) Thermal cyclic aging treatment does not have obvious effect on the EQZ, attributing to the lack of solute elements in the zone.

REFERENCES

1. T. Dursun and C. Soutis: Recent developments in advanced aircraft aluminium alloys. *Mater. Des.* **56**, 862 (2014).
2. J.C. Williams and E.A. Starke: Progress in structural materials for aerospace systems. *Acta Mater.* **51**, 5775 (2003).
3. E.J. Lavernia, T.S. Srivatsan, and F.A. Mohamed: Strength, deformation, fracture behaviour and ductility of aluminium–lithium alloys. *J. Mater. Sci.* **25**, 1137 (1990).
4. A. Ravindra, E.S. Dwarakadasa, T.S. Srivatsan, C. Ramanath, and K.V.V. Iyengar: Electron-beam weld microstructures and properties of aluminium–lithium alloy 8090. *J. Mater. Sci.* **28**, 3173 (1993).
5. P.E. Magnusen, D.C. Mooy, L.A. Yocum, and R.J. Rioja: Development of high toughness sheet and extruded products for airplane fuselage structures. In *ICAA13 Pittsburgh*, H. Weiland, ed. (Springer, Cham, Germany, 2012); p. 353.
6. T.S. Srivatsan and T.S. Sudarshan: Welding of lightweight aluminum–lithium alloys. *Weld. Res. Suppl.* **70**, 173 (1991).
7. R. Xiao and X. Zhang: Problems and issues in laser beam welding of aluminum–lithium alloys. *J. Manuf. Process.* **16**, 166 (2014).
8. Y. Shi, F. Zhong, X. Li, S. Gong, and L. Chen: Effect of laser beam welding on tear toughness of a 1420 aluminum alloy thin sheet. *Mater. Sci. Eng., A* **465**, 153 (2007).
9. L. Cui, X. Li, D. He, L. Chen, and S. Gong: Effect of Nd:YAG laser welding on microstructure and hardness of an Al–Li based alloy. *Mater. Charact.* **71**, 95 (2012).
10. F.M. Ghaini, M. Sheikhi, M.J. Torkamany, and J. Sabbaghzadeh: The relation between liquation and solidification cracks in pulsed laser welding of 2024 aluminium alloy. *Mater. Sci. Eng., A* **519**, 167 (2009).
11. K.H. Hou and W.A. Baeslack: Effect of solute segregation on the weld fusion zone microstructure in CO_2 laser beam and gas tungsten arc welds in Al–Li–Cu alloy 2195. *J. Mater. Sci. Lett.* **15**, 208 (1996).
12. B. Fu, G. Qin, X. Meng, Y. Ji, Y. Zou, and Z. Lei: Microstructure and mechanical properties of newly developed aluminum–lithium alloy 2A97 welded by fiber laser. *Mater. Sci. Eng., A* **617**, 1 (2014).
13. X. Zhang, W. Yang, and R. Xiao: Microstructure and mechanical properties of laser beam welded Al–Li alloy 2060 with Al–Mg filler wire. *Mater. Des.* **88**, 446 (2015).
14. W. Tao, B. Han, and Y. Chen: Microstructural and mechanical characterization of aluminum–lithium alloy 2060 welded by fiber laser. *J. Laser Appl.* **28**, 22 (2016).
15. P.A. Molian and T.S. Srivatsan: Weldability of aluminium–lithium alloy 2090 using laser welding. *J. Mater. Sci. Lett.* **25**, 3347 (1990).
16. Y. Zhang, F. Lu, H. Wang, X. Wang, H. Cui, and X. Tang: Reduced hot cracking susceptibility by controlling the fusion ratio in laser welding of dissimilar Al alloys joints. *J. Mater. Res.* **30**, 993 (2015).
17. A.Y. Ishchenko: High-strength aluminium alloys for welded structures in the aircraft industry. *Weld. Int.* **19**, 173 (2005).
18. K. Chen, W.X. Yang, and R.S. Xiao: Direct laser welding of an Al–Li alloy plate without prior surface cleaning. *Lasers Eng.* **22**, 361 (2011).
19. R. Xiao, W. Yang, and C. Kai: Porosity characterization in laser welds of Al–Li alloy1420. *Appl. Laser* **27**, 13 (2007).
20. I.N. Fridlyander, N.I. Kolobnev, L.B. Khokhlatova, K.H. Rendigs, G. Tempus, A. Haszler, C. Keidel, T. Pfannenmüller, and A.L. Berezina: Structure and properties of sheets of 1424 alloy. *Mater. Sci. Forum* **331–337**, 1393 (2000).
21. W.D. Yong, F.J. Cai, and X.U. Wei: Effect of heat treatment on microstructures and mechanical properties of Al–Li–Cu alloy TIG welded joint. *Rare Metal Mater. Eng.* **42**, 579 (2013).
22. R. Ahmad and M.A. Bakar: Effect of a post-weld heat treatment on the mechanical and microstructure properties of AA6061 joints welded by the gas metal arc welding cold metal transfer method. *Mater. Des.* **32**, 5120 (2011).
23. L. Srinivasan, B.K.T. Deepan, P. Sathiya, and S. Biju: Effect of heat input, heat treatment on microstructure and mechanical properties of GTA welded aerospace material 15CDV6. *J. Mater. Res.* **32**, 1361 (2017).
24. K.Y.S. Wang, C. Chen, and L. Xing: Influence of post-weld heat treatment on microstructure and mechanical properties of Al–Li alloy electron beam welding joint. *Rare Metal Mater. Eng.* **42**, 579 (2013).
25. S. Malarvizhi, K. Raghukandan, and N. Viswanathan: Investigations on the influence of post weld heat treatment on fatigue crack growth behaviour of electron beam welded AA2219 alloy. *Int. J. Fatigue* **30**, 1543 (2008).
26. H. Aydın, A. Bayram, and İ. Durgun: The effect of post-weld heat treatment on the mechanical properties of 2024-T4 friction stir-welded joints. *Mater. Des.* **31**, 2568 (2010).
27. C. Li, H.Y. Ding, C. Li, H.E. En-Guang, and G.U. Chang-Shi: Effects of post-weld heat treatment on microstructure of laser welded joints in an Al–Li alloy. *Trans. Mater. Heat Treat.* **35**, 58 (2014).
28. L. Xu, Z. Tian, Y. Peng, and X. Zhang: Laser-MIG hybrid welding on high strength aluminum alloy. *Chin. J. Rare Met.* **29**, 773 (2005).
29. W.S. Su Diyao and J. Huijin: Effects of aging treatments on microstructure and micro-hardness of 2219-T87 welds. *J. Aeronaut. Mater.* **35**, 49 (2015).
30. J. Li, Y. Chen, X. Zhang, P. Liu, and C.S. University: Influence of non-isothermal aging on microstructures and mechanical properties of Al–Li alloy. *Rare Met. Mater. Eng.* **46**, 183 (2017).
31. A. Gutierrez and J.C. Lippold: A proposed mechanism for equiaxed grain formation along the fusion boundary in aluminum–copper–lithium alloys. *Weld. J.* **77**, 123 (1998).
32. S.F. Zhang, W.D. Zeng, W.H. Yang, C.L. Shi, and H.J. Wang: Ageing response of a Al–Cu–Li 2198 alloy. *Mater. Des.* **63**, 368 (2014).
33. S. Ahmadi, H. Arabi, and A. Shokuhfar: Formation mechanisms of precipitates in an Al–Cu–Li–Zr alloy and their effects on strength and electrical resistance of the alloy. *J. Alloys Compd.* **484**, 90 (2009).
34. J.C. Huang and A.J. Ardell: Addition rules and the contribution of δ′ precipitates to strengthening of aged Al–Li–Cu alloys. *Acta Metall.* **36**, 2995 (1988).
35. K.S. Kumar, S.A. Brown, and J.R. Pickens: Microstructural evolution during aging of an Al–Cu–Li–Ag–Mg–Zr alloy. *Acta Mater.* **44**, 1899 (1996).
36. Z. Zhao, X. Li, L. Xu, and D. Han: Strengthening effect of T1 precipitates and influence of minor cerium in 2090 Al–Li alloys. *Chin. J. Nonferrous Met.* **9**, 546 (1999).
37. H. Sidhar and R.S. Mishra: Aging kinetics of friction stir welded Al–Cu–Li–Mg–Ag and Al–Cu–Li–Mg alloys. *Mater. Des.* **110**, 60 (2016).
38. P. Lequeu, K.P. Smith, and A. Daniélou: Aluminum–copper–lithium alloy 2050 developed for medium to thick plate. *J. Mater. Eng. Perform.* **19**, 841 (2010).

39. R. Yoshimura, T.J. Konno, E. Abe, and K. Hiraga: Transmission electron microscopy study of the early stage of precipitates in aged Al–Li–Cu alloys. *Acta Mater.* **51**, 2891 (2003).
40. W.Y. Chen Zheng, D. Zhanlai, and Z. Zhilong: Mechanism of extrinsic strengthening and instrinsic toughening for aluminium–lithium alloy containing rare earth element. *J. Chin. Soc. Rare Earths.* **19**, 23 (1998).
41. B. Han, W. Tao, Y. Chen, and H. Li: Double-sided laser beam welded T-joints for aluminum–lithium alloy aircraft fuselage panels: Effects of filler elements on microstructure and mechanical properties. *Opt. Laser Technol.* **93**, 99 (2017).
42. A. Kostrivas and J.C. Lippold: Weldability of Li-bearing aluminum alloys. *Int. Mater. Rev.* **44**, 217 (1999).
43. A. Kostrivas and J.C. Lippold: Fusion boundary microstructure evolution in aluminium alloys. *Weld. World* **50**, 24 (2006).